

1           **Evaluation of atmospheric model parameterization  
2           schemes with river network routing and streamflow  
3           observations: A case study of the Yarlung Zangbo  
4           River on the Tibetan Plateau**

5           **Heng Yang<sup>1</sup>, Shuanglong Chen<sup>2</sup>, Qingyun Bian<sup>3</sup>, and Hui Zheng<sup>3</sup>**

6           <sup>1</sup>Science and Technology Research Institute, China Three Gorges Corporation, Beijing 100038, China

7           <sup>2</sup>Baihetan Hydropower Plant, China Three Gorges Corporation, Sichuan 615421, China

8           <sup>3</sup>Institute of Atmospheric Physics, Chinese Academy of Sciences, Beijing 100029, China

9           **Key Points:**

- 10           • A river network routing-based method is developed to evaluate atmospheric mod-  
11           els using streamflow observations
- 12           • High skill in streamflow correlation coefficient corresponds to superiority in mod-  
13           eling the spatial distribution of precipitation
- 14           • Shortwave radiation parameterization has a minimal impact on precipitation es-  
15           timation but a notable impact on runoff and streamflow

**Abstract**

Evaluating kilometer-scale atmospheric models in data-sparse regions with complex topography, such as the Tibetan Plateau, presents inherent challenges due to the scarcity of in-situ observations and uncertainties in remote-sensing data. Hydrological evaluations, which utilize hydrological models to connect atmospheric model-simulated precipitation with streamflow observations, are hindered by model structural and parameter uncertainties, particularly significant in high-altitude mountainous basins. This study introduces a river network routing-based method that calculates streamflow directly from atmospheric model-simulated runoff, making fewer assumptions and thus being more adaptable to high-altitude mountainous basins. We applied this method to assess 3-kilometer Weather Research and Forecasting (WRF) model simulations over the Yarlung Zangbo River on the Tibetan Plateau, each configured with distinct parameterizations for microphysics, planetary boundary layer, and shortwave radiation. The streamflow evaluation was compared with an evaluation of precipitation against satellite data. Results indicate that the streamflow evaluation complements the precipitation evaluation effectively. The experiment that excelled in reproducing precipitation amounts and temporal variations also demonstrated the best performance in estimating streamflow's mean and variability. Furthermore, the river routing-based evaluation of streamflow offers additional insights beyond the precipitation evaluation. While the shortwave radiation parameterization had negligible impacts on precipitation amount, its influence on streamflow was significant. The experiment utilizing the Dudhia radiation scheme achieved the best temporal correlation with streamflow observations, corresponding to an accurate representation of spatial precipitation patterns as evaluated against satellite data. The findings underscore the value of the river network routing-based method in evaluating atmospheric models, especially in data-sparse and topographically complex regions.

**1 Introduction**

In recent years, the resolution of atmospheric models has gradually increased, with grid spacings now reaching kilometers or less (P. Clark et al., 2016; Prein et al., 2015; Stevens et al., 2019; Tang et al., 2023; L. Li et al., 2024). These high-resolution, kilometer-scale models have largely overcome the need for deep convection parameterizations, thereby eliminating a significant source of uncertainty that was previously inherent in coarser-resolution models (Prein et al., 2015; P. Clark et al., 2016; Mooney et al., 2017). More-

48 over, kilometer-scale atmospheric simulations are capable of capturing the intricate ef-  
49 fects of fine-scale topography on atmospheric circulation patterns, particularly in moun-  
50 tainous regions (C. Lin et al., 2018; Zhou et al., 2021; Yuan et al., 2023; Sugimoto et al.,  
51 2021; Ma et al., 2023; G. Li et al., 2022). The explicit representation of deep convection  
52 and meticulous attention to topographic detail have substantially enhanced the accu-  
53 racy of the estimation of hydrological gradients along terrain slopes (Jiang, Yang, Yang,  
54 et al., 2022; Sugimoto et al., 2021; Ma et al., 2023).

55 In mountainous regions characterized by strong hydrological gradients, such as the  
56 Tibetan Plateau, kilometer-scale atmospheric models are particularly useful (Prein et  
57 al., 2023). Mountainous regions experience pronounced hydrological gradients (Immerzeel  
58 et al., 2014) that are undergoing substantial changes due to global climate change (Yao  
59 et al., 2019; Cui et al., 2023; T. Wang et al., 2021; Kraaijenbrink et al., 2021). The scarcity  
60 of in-situ observations and the inherent uncertainties in remote-sensing products impede  
61 the accurate monitoring of these hydrological changes (Miao et al., 2024). Evidence sug-  
62 gests that kilometer-scale atmospheric models can achieve an accuracy that surpasses  
63 that of in-situ observations (Lundquist et al., 2019) and even satellite-based products (Jiang,  
64 Yang, Li, et al., 2022). Moreover, these models are indispensable for projecting future  
65 water resources in the context of a changing climate (Prein et al., 2023).

66 In mountainous regions, the accurate evaluation of kilometer-scale atmospheric mod-  
67 els presents a formidable challenge. Meteorological observations are frequently confined  
68 to select locations within river valleys, leaving vast areas unmonitored. Remote locales,  
69 such as mountain peaks and barren lands, are known to contribute significantly to wa-  
70 ter sources but are often overlooked in observational data (Miao et al., 2024). The com-  
71 plex topography and frozen ground in these areas can significantly distort remote-sensing  
72 products, including satellite-based precipitation estimates (Behrangi et al., 2014). Con-  
73 sequently, the scarcity of in-situ meteorological observations and the associated uncer-  
74 tainties in remote-sensing data render the assessment of kilometer-scale atmospheric mod-  
75 els less conclusive.

76 Hydrological evaluation serves as an enlightening approach for assessing the per-  
77 formance of atmospheric models in mountainous regions. This technique involves uti-  
78 lizing the precipitation data simulated by an atmospheric model to drive a hydrologi-  
79 cal model. Subsequently, the resulting streamflow is compared against observed stream-

flow (Krier et al., 2012; Henn et al., 2015, 2016; Pang et al., 2020). However, the application of a hydrological model requires a significant array of assumptions concerning model structure and parameterization (Kirchner, 2009; Henn et al., 2016). These assumptions can be conveniently tested in data-rich regions (M. P. Clark et al., 2011; Zheng et al., 2020), but they remain largely unconstrained in data-sparse regions, such as the Tibetan Plateau. There exists the potential for such uncertainties to be so pronounced that distinguishing the simulated precipitation from the observed streamflow becomes an ill-posed problem (Renard et al., 2010). Different combinations of precipitation and hydrological models may yield similar streamflows that align with observations. Due to the significant uncertainty inherent in hydrological models and limited fidelity constraints in such cases, the inclusion of low-fidelity hydrological models in the evaluation process, particularly when they contribute to the best streamflow estimates, may inadvertently lead to an erroneous assessment of the atmospheric model's performance. This concern is particularly pertinent to high-altitude mountainous basins, such as the Yarlung Zangbo River basin, where considerable model structural and parameter uncertainty has been found in our previous study (Lei et al., 2025).

Hydrological models primarily capture two fundamental processes in mountainous basins: runoff generation and water flow routing. Despite the intricate nature of runoff-generation processes in mountainous regions (van Tiel et al., 2024), the routing processes are often less complex than those observed over flat terrains (Getirana & Paiva, 2013; Moussa & Bocquillon, 1996). Characterized by steep slopes, mountain rivers and terrains enable water flow to be primarily represented using the kinematic wave approximation of the Saint-Venant equations (Moussa & Bocquillon, 1996) (channel routing) or the shallow water equations (terrain routing). This representation indicates that the water flow is predominantly influenced by the interplay between friction and terrain slope (Getirana & Paiva, 2013; Moussa & Bocquillon, 1996). Given that terrain slopes can be extracted globally from high-resolution digital elevation models (Yamazaki et al., 2017, 2019), the routing of water flow in mountainous basins is heavily reliant on assumptions about friction. While the friction assumption makes a relatively minor component within the previously discussed hydrological models, characterizing uncertainties in friction is often more straightforward than addressing the structural and parameter uncertainties inherent to hydrological models. The simplicity and robustness of the routing process in mountainous basins enhance its adaptability for evaluating atmospheric models in these regions.

113 In light of the aforementioned findings, we propose an alternative approach to eval-  
114 uating atmospheric models that leverages river network routing. This approach involves  
115 directly routing the runoff simulated by atmospheric models through the river network  
116 to generate streamflow estimates at gauge locations. The method streamlines the eval-  
117 uation process by circumventing the complexities of runoff generation processes, which  
118 are now integrated within the atmospheric model. Atmospheric models are better quipped  
119 to constrain the runoff generation processes than hydrological models, due to their abil-  
120 ity to account for surface energy and water balance dynamics as well as land-atmosphere  
121 interactions (Wagner et al., 2016; Senatore et al., 2015). We contend that this river net-  
122 work routing-based method is particularly well-suited for data-sparse and topograph-  
123 ically complex regions such as the Tibetan Plateau, providing a more targeted and ef-  
124 fective means of model evaluation.

125 In this study, we have implemented our proposed method to evaluate the simula-  
126 tions produced by the Weather Research and Forecasting (WRF) model (Powers et al.,  
127 2017), specifically applied to the Yarlung Zangbo River, the most significant river on the  
128 Tibetan Plateau. The structure of this paper is as follows: Section 2 delineates the method-  
129 ologies and datasets utilized in our research. Section 3 details the outcomes, and discus-  
130 sions follow in Section 4. Finally, Section 5 synthesizes the findings and concludes the  
131 study.

## 132 2 Methods and Data

### 133 2.1 Experimental Design

134 Figure 1 illustrates the workflow of this study. We conducted a series of five 3-kilometer  
135 WRF experiments from May 1 to October 1, 2013, encompassing the wet season of the  
136 year. The first 50 days were used for spin-up, and the simulations from June 20 to Oc-  
137 tober 1 were analyzed. The experiments were configured with various parameterization  
138 schemes for cloud physics, planetary boundary layer, and shortwave radiation. The ob-  
139 jective was to identify the optimal parameterization scheme using streamflow observa-  
140 tions from four river gauges on the main stem of the Yarlung Zangbo River, namely, Lazi,  
141 Nugesha, Yangcun, and Nuxia, arranged from upstream to downstream.

142 The WRF experiments were initialized and driven by data from the European Cen-  
143 tre for Medium-Range Weather Forecasts Reanalysis version 5 (ERA5) (Hersbach et al.,

144 2020). The runoff simulated by WRF was then spatially re-mapped to account for lat-  
145 eral inflow into the river network. The river flow within this network was subsequently  
146 routed using the Muskingum method, a well-established approach for routing mountain-  
147 ous river flows. We tested a range of routing parameter values, calibrating them against  
148 streamflow observations to identify the optimal value for each segment of the river net-  
149 work situated between two river gauges. Finally, the WRF experiments were intercom-  
150 pared and assessed based on the accuracy of streamflow estimation using these optimal  
151 routing parameters.

## 152 2.2 Observational Data

153 We utilized streamflow data provided by the China Three Gorges Corporation, col-  
154 lected at four river gauges: Lazi, Nugesha, Yangcun, and Nuxia. Instantaneous stream-  
155 flow observations were recorded daily at 00:00 UTC from June 20 to October 1, 2013.  
156 These data were instrumental in optimizing the routing parameter and evaluating the  
157 estimated streamflow for the WRF experiments.

158 To intercompare the river network routing-based evaluation of streamflow with the  
159 widely adopted precipitation evaluations based on remote sensing products, we also em-  
160 ployed the Global Precipitation Measurement (GPM) Multi-satellitE Retrievals for GPM  
161 (IMERG) product (Huffman et al., 2019). The IMERG product provides data at a spa-  
162 tial resolution of 0.1° by 0.1° and a temporal resolution of 30 minutes. We applied bi-  
163 linear interpolation to downscale the GPM data to align with the 3-kilometer resolution  
164 of the WRF grid.

## 165 2.3 Study Area and River Network

166 Figure 2 displays the modeling domain of the WRF model, which spans 380 by 660  
167 grid cells, each measuring 3 by 3 kilometers. The domain covers the entire Yarlung Zangbo  
168 River basin and extends to include a buffer zone surrounding the river basin. This buffer  
169 zone, which is over 200 kilometers wide, is strategically designed to allow for the devel-  
170 opment of small-scale weather systems before they interact with the river basin (Denis  
171 et al., 2002). This design helps to mitigate the adverse effects stemming from inaccu-  
172 rate or low-resolution boundary conditions.

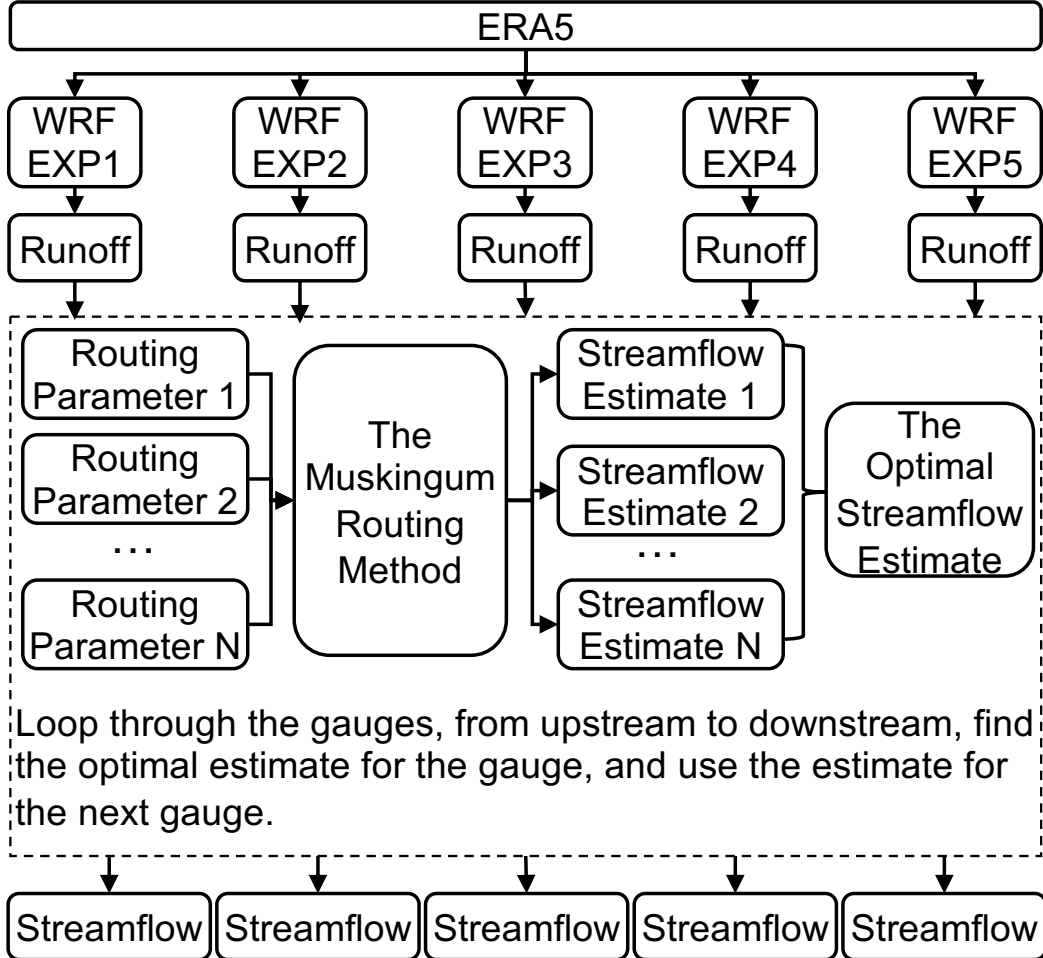


**Figure 1.** Schematic diagram of the workflow of this study. The parameterization schemes used in the WRF experiments are listed in Table 1.

173        The routing was performed on the river network as illustrated in Figure 2. The river  
 174        network was delineated from the Multi-Error Removed Improved-Terrain Hydrography  
 175        (MERIT-Hydro) dataset (Yamazaki et al., 2017, 2019), which offers flow directions and  
 176        accumulative upstream area data at a spatial resolution of 3 by 3 arcseconds. The de-  
 177        lineation process unfolds in three sequential steps: Initially, the accumulative upstream  
 178        area is employed to identify river centerlines, with a grid cell being classified as such if  
 179        its accumulative upstream area exceeds  $10 \text{ km}^2$ . Subsequently, these centerlines are seg-  
 180        mented into river reaches from upstream to downstream, defining a reach by an increase  
 181        in the accumulative upstream area of at least  $20 \text{ km}^2$  along its path. Finally, the flow  
 182        direction data are utilized to determine the catchment area of each reach, encompass-  
 183        ing all grid cells that contribute flow directly to the reach. The thresholds for defining

184 river centerlines and segmenting river reaches align with those used in previous large-  
 185 domain river routing studies (P. Lin et al., 2021, 2019). This delineation process results  
 186 in a fully connected river network consisting of 5,800 reaches, with an average catchment  
 187 area of 33 km<sup>2</sup>.

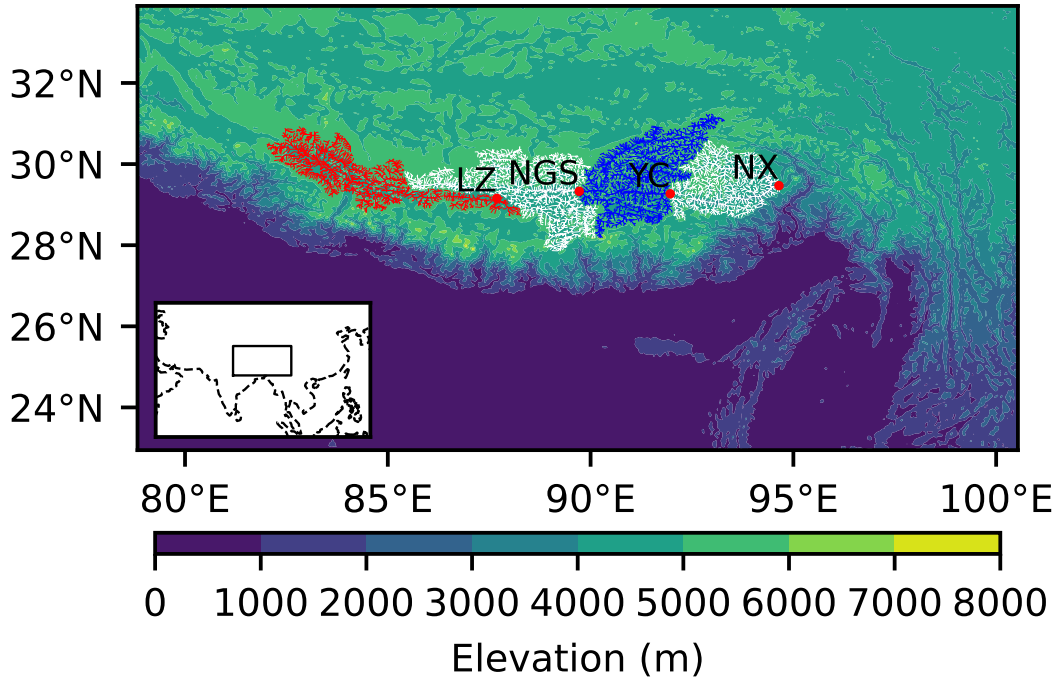


**Figure 2.** Modeling domain and delineated river network of the Yarlung Zangbo River. The colormap provides a representation of the terrain elevation, showcasing the basin's topographical characteristics. Red dots indicate the locations of the four river gauges along the river's course, labeled as follows: LZ for Lazi, NGS for Nugesha, YC for Yangcun, and NX for Nuxia from upstream to downstream. The differently colored lines correspond to the river reaches that lie between consecutive gauges, offering a visual guide to their spatial distribution across the basin. The inset illustrates the study domain, depicted as a rectangle, along with the coastlines, which are represented by dashed lines.

#### 188 2.4 WRF Parameterization Schemes

189 Table 1 lists the parameterization schemes chosen from WRF version 4.3.1 for the  
 190 experiments. EXP1 serves as the baseline experiment, configured similarly to the High  
 191 Asian Refined Analysis version 2 (X. Wang et al., 2021) with the exception of the ra-  
 192 diation and land surface processes. Instead of the Rapid Radiative Transfer Model (RRTM)

scheme (Mlawer et al., 1997), the RRTM for GCMs (RRTMG) (Iacono et al., 2008) was employed for shortwave and longwave radiation transfer. RRTMG is comparable to RRTM in terms of modeling radiative forcing but offers greater computational efficiency (Iacono et al., 2008). For the land surface processes, the Noah land surface model with multi-parameterization options (Noah-MP) (Niu et al., 2011; Z.-L. Yang et al., 2011) was selected in place of the Noah model used in HARR version 2. Noah-MP has been enhanced over the original Noah model, providing an improved representation of snow and runoff processes (Niu et al., 2011). These enhancements have led to better performance in modeling runoff (Liang et al., 2019; Zheng et al., 2023), leading to the widespread adoption of Noah-MP in hydrological applications (Cosgrove et al., 2024; P. Lin, Hopper, et al., 2018). The Noah-MP model includes several different parameterization options for runoff generation. In this study, we utilized the Noah runoff scheme, which employs an exponentially distributed infiltration capacity for runoff generation (Schaake et al., 1996). This scheme also assumes free drainage at the bottom of the soil column to simulate subsurface runoff.

EXP2 through EXP5 are configured based on EXP1 by altering the parameterization schemes one at a time. EXP2 and EXP3 vary from EXP1 in the choice of cloud microphysics scheme. EXP1 employs the Thompson scheme (Thompson et al., 2008), whereas EXP2 utilizes the Purdue Lin scheme (S.-H. Chen & Sun, 2002), and EXP3 incorporates the WRF Single-Moment 6-Class Microphysics (WSM6) scheme (Hong & Lim, 2006). EXP4 diverges from EXP1 in its planetary boundary layer scheme. Instead of the Mellor-Yamada-Janjić scheme (Janjić, 1994), EXP4 adopts the Yonsei University scheme (Hong et al., 2006). EXP5 differs from EXP1 in its radiation scheme, opting for the Dudhia scheme (Dudhia, 1989) for shortwave radiation transfer. These experiments are designed to investigate the impacts of cloud microphysics, planetary boundary layer, and shortwave radiation, as these parameterizations have demonstrated their significance in previous studies (Lv et al., 2020; Prein et al., 2023).

## 220 2.5 River Network Routing Method

221 The WRF model includes a routing module called WRF-Hydro (P. Lin, Yang, et  
 222 al., 2018; Givati et al., 2016). WRF-Hydro is a comprehensive model that integrates sub-  
 223 surface runoff, soil moisture redistribution, diffusive terrain routing, and Muskingum–  
 224 Cunge river routing. However, its complexity introduces a large number of parameter-

**Table 1.** WRF experiments and the used parameterization schemes.

Experiment	Cloud Microphysics	Planetary Boundary Layer	Shortwave Radiation
EXP1	Thompson	MYJ	RRTMG
EXP2	Purdue Lin	MYJ	RRTMG
EXP3	WSM6	MYJ	RRTMG
EXP4	Thompson	YSU	RRTMG
EXP5	Thompson	YSU	Dudhia

ization options and parameters, making thorough calibration challenging (RafieeiNasab et al., 2025), particularly in data-sparse regions such as the Yarlung Zangbo River basin (Lei et al., 2025). Undercalibration of the routing model can introduce biases in the evaluation of atmospheric model parameterizations.

As described in the Introduction, routing processes in mountainous regions can be substantially simplified. In alignment with our study purpose and the aforementioned reasoning, we opted for Muskingum routing over a dense river network instead of WRF-Hydro. A dense river network serves not only as a prescribed water flow path for river routing but also, to some extent, as a surrogate for terrain routing. If the river network is sufficiently dense, terrain routing within small catchments with steep slopes can be neglected. This simplification significantly reduces the number of parameters to be calibrated, making the study computationally feasible and robust in its evaluation results.

The WRF-simulated runoff is re-mapped to represent lateral inflow into the river network, following the remapping method detailed in (P. Lin, Yang, et al., 2018; S. Wang et al., 2019). Unlike P. Lin, Yang, et al. (2018), we identified all WRF grid cells that intersect with the catchment of a river reach, rather than using a single grid cell at the centroid of the catchment. The runoff volume from these grid cells is then calculated by multiplying the runoff depth by the area of intersection for each cell. These individual values are subsequently summed to determine the total lateral flow volume entering the reach. This method conserves the total runoff volume despite variations in river network geometry.

The Muskingum method is well-suited to characterize flow's kinematic wave propagation that driven by the topographic gradient (Ponce et al., 1978). The formulation of the Muskingum method (Cunge, 1969; Fenton, 2019), when incorporating lateral inflows, can be expressed as follows:

$$Q_i^t = \frac{k - x}{1 - x + k} Q_{i-1}^t + \frac{1 - x - k}{1 - x + k} Q_i^{t-1} + \frac{x + k}{1 - x + k} Q_{i-1}^{t-1} + \frac{2k}{1 - x + k} Q_l^t, \quad (1)$$

$$k = \frac{c\Delta t}{2\Delta l}, \quad (2)$$

where  $Q_i^t$  ( $\text{m}^3 \text{s}^{-1}$ ) is the streamflow of a reach at current time step,  $Q_{i-1}^t$  ( $\text{m}^3 \text{s}^{-1}$ ) is the streamflow at the upstream position of the reach at current time step,  $Q_i^{t-1}$  ( $\text{m}^3 \text{s}^{-1}$ ) is the streamflow of the reach at previous time step,  $Q_{i-1}^{t-1}$  ( $\text{m}^3 \text{s}^{-1}$ ) is the streamflow at the upstream position at the previous time step,  $Q_l^t$  ( $\text{m}^3 \text{s}^{-1}$ ) is the lateral inflow entering the reach at current time step.  $\Delta t$  is the time step (s), and  $\Delta l$  is the reach length (m).

$x$  is the weighting factor (unitless), and  $c$  is the wave celerity ( $\text{m s}^{-1}$ ).

The application of the Muskingum method to the reaches of a fully connected river network must be executed in the correct order. When routing the streamflow of a reach, the discharge at the reach's upstream position must be available. We sorted all the river reaches within the network according to the stream order as introduced in (X. Yang et al., 2024). This sorting ensures that upstream reaches are always prioritized over their downstream counterparts. Subsequently, we apply the Muskingum method to each reach in the established sequence. This sequence guarantees that routing on upstream reaches is conducted first, followed by routing on downstream reaches.

The Muskingum method includes two adjustable routing parameters: the weighting factor ( $x$ ; unitless) and wave celerity ( $c$ ;  $\text{m s}^{-1}$ ). The weighting factor  $x$  is used to regulate the proportional contributions of the right-hand-side terms in Equation 1. Studies have shown that the simulated streamflow is relatively insensitive to variations in the weighting factor (Koussis, 1978). Values ranging from 0.1 to 0.3 are typically effective for most streams. Guided by the experiments reported by David et al. (2011), we have chosen a parameter value of 0.3 for this study.

The wave celerity  $c$  represents the speed at which the flow wave propagates downstream. It is influenced by the physical characteristics of the river channel, including channel slope, roughness, and width. Given that direct observations of  $c$  are unavailable for the Yarlung Zangbo River basin, we conducted a series of simulations with varying wave celerity values. We selected the value that best aligns with the streamflow observations,

which is considered representative of the river channel's physical characteristics. The optimal wave celerity value  $c$  is determined for each streamflow gauge in an upstream-to-downstream sequence. Once a wave celerity value is chosen for a gauge, it is applied to all downstream gauges. This process is repeated sequentially until wave celerity values are selected for all streamflow gauges.

## 2.6 Evaluation Metrics

We utilized the Pearson correlation coefficient to identify the optimal wave celerity value. The Pearson correlation coefficient ( $r$ ) is defined as follows:

$$r = \frac{\sum_{i=1}^n (x_i - \bar{x})(y_i - \bar{y})}{\sqrt{\sum_{i=1}^n (x_i - \bar{x})^2 \sum_{i=1}^n (y_i - \bar{y})^2}}, \quad (3)$$

where  $x_i$  and  $y_i$  are the simulated and observed streamflow at time step  $i$ , respectively.  $\bar{x}$  and  $\bar{y}$  are the mean of the simulated and observed streamflow, respectively. The Pearson correlation coefficient ranges from  $-1$  to  $1$ , with a value of  $1$  indicating a perfect positive linear relationship between the simulated and observed streamflow. This coefficient is insensitive to biases in the streamflow estimates, making us to focus on daily scale streamflow variations in this study.

We used the Kling–Gupta efficiency (KGE) (Gupta et al., 2009) to intercompare the WRF parameterization schemes. KGE systematically summarizes how a hydrological simulation matches observations in correlation, standard deviation, and bias. The KGE is defined as follows:

$$\text{KGE} = 1 - \sqrt{(r - 1)^2 + (\alpha - 1)^2 + (\beta - 1)^2}, \quad (4)$$

$$\alpha = \frac{\sigma}{\sigma_o}, \quad (5)$$

$$\beta = \frac{\mu_s}{\mu_o}, \quad (6)$$

where  $r$  is the Pearson correlation coefficient between the simulation and observation,  $\sigma$  is the standard deviation of the simulation, and  $\mu$  is the mean. The subscripts  $s$  and  $o$  denote the simulated and observed values, respectively. The KGE ranges from  $-\infty$  to  $1$ . A KGE value of  $1$  indicates a perfect match between the simulated and observed streamflow.

299      **3 Results**

300      In this section, we first intercompares the WRF-simulated precipitation and runoff.  
 301      Subsequently, we assess the streamflow estimates by comparing them against observed  
 302      streamflow data.

303      **3.1 Intercomparison of the WRF-simulated precipitation and runoff**

304      Figure 3 displays the spatial distribution of simulated precipitation from the five  
 305      WRF experiments. The patterns from EXP1 through EXP3 exhibit close agreement, with  
 306      two primary precipitation centers evident downstream of Yangcun and between Lazi and  
 307      Nugesha. Notably, the precipitation intensity between Lazi and Nugesha is slightly higher.  
 308      In comparison to the baseline EXP1, the distribution in EXP5 appears more dispersed,  
 309      featuring a significant precipitation center downstream of Yangcun, as shown in Figure 3e.  
 310      EXP4 closely mirrors the spatial pattern of EXP5, with a spatial correlation coefficient  
 311      of 0.93 achieved between them. However, EXP4 (Figure 3d) exhibits the weakest pre-  
 312      cipitation intensity among the experiments. The experiments show greater consensus in  
 313      the downstream areas of the Yarlung Zangbo River than in the headwater regions, as  
 314      indicated in Figure 3f. When juxtaposed with the GPM data, there is a tendency for all  
 315      five experiments to overestimate the precipitation rate. Intercomparison among the ex-  
 316      periment suggests that the planetary boundary layer parameterization scheme substan-  
 317      tially influences the simulated precipitation, particularly in the western upstream areas.  
 318      The results is consistent with the findings from the Coordinated Regional Climate Down-  
 319      scaling Experiment (CORDEX) Convection-Permitting Third Pole (CPTP) project (Prein  
 320      et al., 2023). Kilometer-scale simulations have revealed the presence of easterly winds  
 321      in the lower boundary layer on the Tibetan Plateau. Biases in the boundary layer winds  
 322      would lead to systematic errors in the simulation (Kukulies et al., 2023).

323      Figure 4 presents the time series of accumulated precipitation, averaged across the  
 324      drainage basin (i.e., all the upstream grid cells) of the four river gauges. Consistent with  
 325      the spatial distribution depicted in Figure 3, all five WRF experiments exceed the GPM  
 326      IMERG precipitation rate across all four drainage basins. The variation among the ex-  
 327      periments is considerable. The disparity between EXP4 and EXP1 underscores the sig-  
 328      nificant influence of the planetary boundary layer on precipitation. This finding aligns  
 329      with the results reported by Prein et al. (2023), suggesting that the impact of planetary

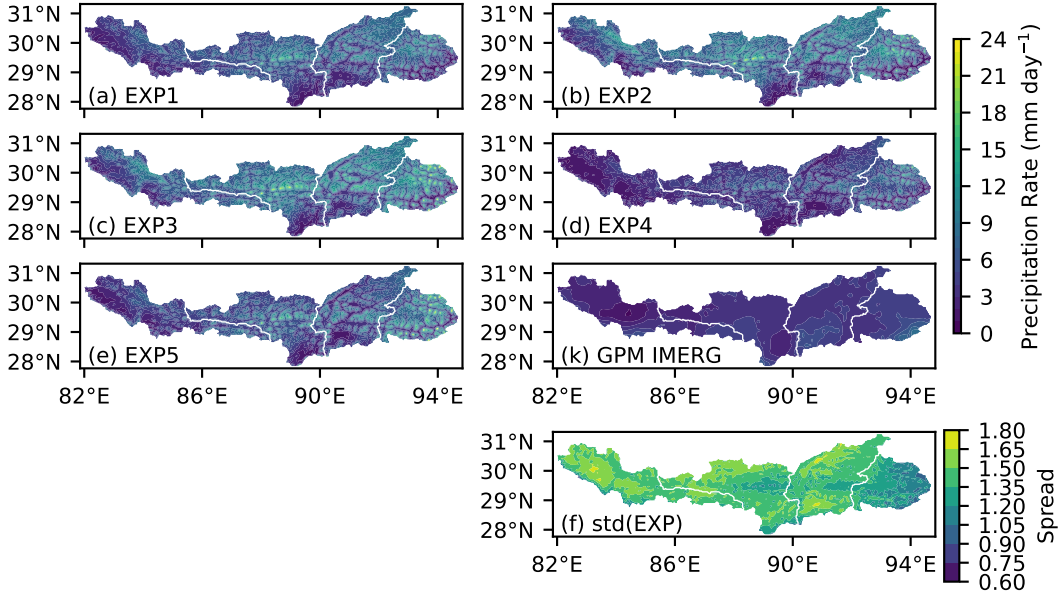


**Figure 3.** Spatial distribution of the precipitation rate averaged from June 20 to October 1, 2013. (a)–(e) The five WRF experiments described in Table 1. (k) The GPM IMERG precipitation. (f) the ensemble spread of the five experiments measured in standard deviation. The white lines denotes the division of the river network between the river gauges.

boundary layer parameterization can be more pronounced than that of cloud physics, as evidenced by the differences between EXP1 and EXP2, and between EXP1 and EXP3. The difference between EXP5 and EXP1 is negligible across all four drainage basins, indicating that the parameterization of shortwave radiation has a minimal impact on the simulation of precipitation.

Table 2 presents the skill of the WRF experiments as measured against GPM data. The cloud physics parameterization significantly influences the timing of precipitation, leading to substantial changes in the correlation coefficient ( $r$ ) for EXP2 and EXP3 relative to EXP1. A comparison between EXP4 and EXP1 indicates that the planetary boundary layer parameterization has a minimal impact on precipitation timing. However, there are notable differences in the amount of precipitation ( $\beta$ ) and its variability ( $\alpha$ ), suggesting the importance of the planetary boundary layer in moisture transport for precipitation (Y. Wang et al., 2020). Although the shortwave radiation parameterization has a minimal impact on the amount of precipitation ( $\beta$ ), it significantly affects the magnitude of precipitation variability ( $\alpha$ ), particularly in the middle reaches of the Yarlung

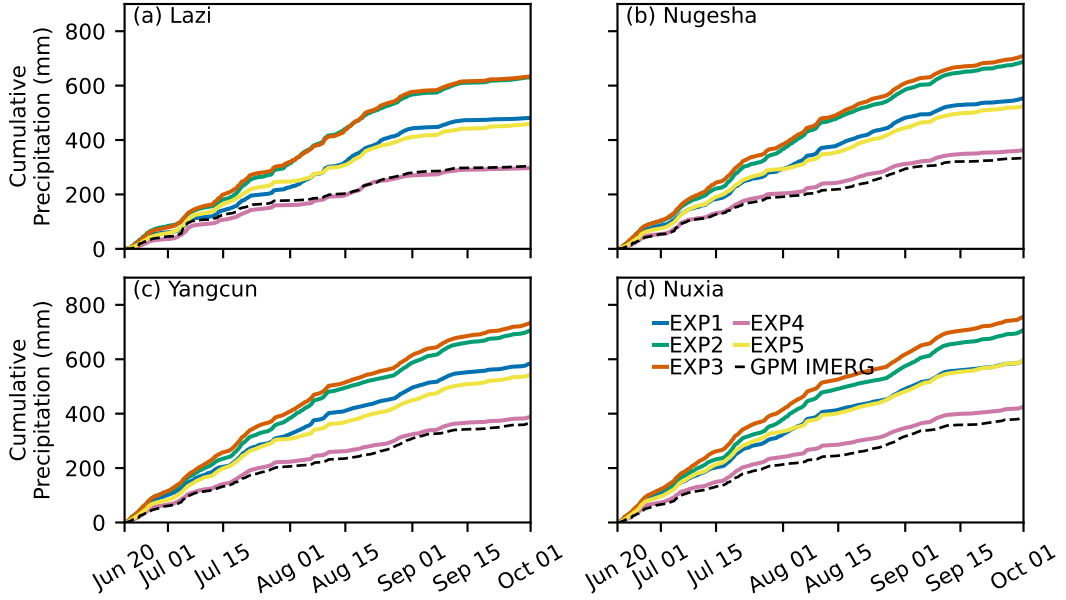


**Figure 4.** Time series in the accumulated precipitation averaged over the drainage basin of (a) Lazi, (b) Nugesha, (c) Yangcun, and (d) Nuxia.

Zangbo River between Lazi and Yangcun. The reason for this impact is not yet clear. However, offline studies in this area (Lei et al., 2025) have found that shortwave radiation significantly affects the land surface energy and water budgets. We hypothesize that the changes in precipitation may be a consequence of local land-atmosphere interactions originated from the changes in land surface energy budgets.

Figure 5 presents the time series of accumulated runoff, averaged across the drainage basins of the four river gauges. The accumulated runoff for the specified period correlates well with the precipitation data. The accumulated runoff for the specified period exhibits a strong correlation with the precipitation data. Among the five experiments, EXP2 and EXP3 produce the highest runoff estimates, with their performances being closely aligned. In contrast, EXP4 records the lowest runoff, and its deviation from EXP1 is more significant than the difference observed between EXP1 and EXP2. The disparity in runoff between EXP5 and EXP1 is considerably larger than the difference in their respective precipitation estimates, especially in the upper reaches of the Yarlung Zangbo River, as shown in Figures 5b and 5c. This pronounced difference in runoff is anticipated to result in variations in the streamflow estimates, which will be further analyzed in the subsequent sections.

**Table 2.** Kling–Gupta efficiency of the hourly precipitation rate averaged within the drainage basin of the river gauges. Italic fonts indicate the experiment that best matches GPM.

	Metric	LZ	NGS	YC	NX
EXP1	KGE	0.32	0.25	0.30	0.36
	$\alpha$	1.06	1.22	1.22	1.22
	$\beta$	1.58	1.66	1.60	1.55
	$r$	0.65	0.72	0.73	0.75
EXP2	KGE	−0.23	−0.22	−0.10	0.00
	$\alpha$	1.27	1.39	1.37	1.37
	$\beta$	2.07	2.06	1.94	1.85
	$r$	0.46	0.53	0.56	0.60
EXP3	KGE	−0.19	−0.23	−0.12	−0.07
	$\alpha$	1.22	1.36	1.34	1.34
	$\beta$	2.08	2.12	2.01	1.97
	$r$	0.58	0.65	0.67	0.69
EXP4	KGE	0.61	0.72	0.73	0.75
	$\alpha$	0.75	0.94	0.94	0.97
	$\beta$	0.98	1.09	1.07	1.11
	$r$	0.70	0.74	0.75	0.77
EXP5	KGE	0.39	0.35	0.42	0.38
	$\alpha$	0.94	1.11	1.09	1.14
	$\beta$	1.51	1.57	1.49	1.55
	$r$	0.67	0.72	0.71	0.74

### 3.2 Evaluation against streamflow observations

Figure 6 illustrates the changes in the correlation coefficient of streamflow with celerity across the four river gauges. Table 3 lists the optimal celerity values for each gauge

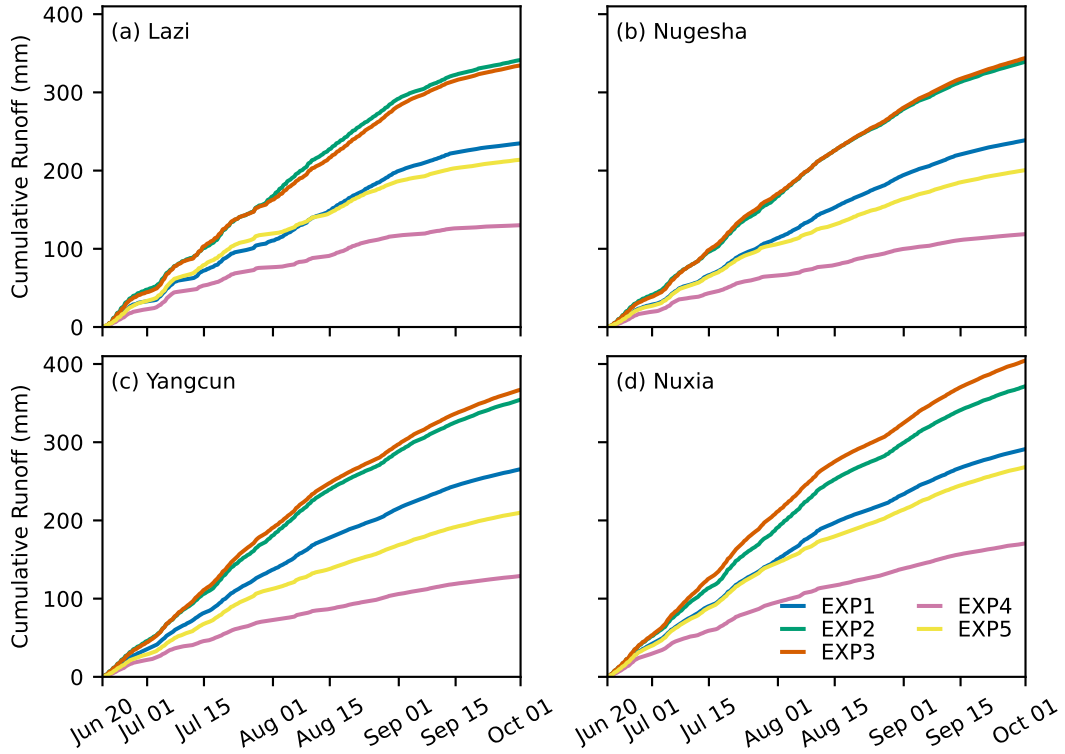


**Figure 5.** Time series of the accumulated runoff averaged over the drainage area of (a) Lazi, (b) Nugesha, (c) Yangcun, and (d) Nuxia.

corresponding to the WRF experiments. The variation of the correlation coefficient with celerity and the optimal celerity values exhibit consistency across all five experiments. This consistency supports the hypothesis that celerity is predominantly determined by the river channel characteristics in mountainous basins. Specifically, the optimal celerity in the upstream segment of the main channel is generally slower compared to that in the downstream segment. As shown in Figure 2, the downstream area, located at the edge of the Tibetan Plateau, is characterized by a broader river channel and a steeper slope. These characteristics likely contribute to the observed differences in celerity.

Figure 7 displays the time series of streamflow estimates for the five WRF experiments at the four river gauges. Table 4 provides a detailed assessment of the skill of these estimations. Consistent with the observations in precipitation and runoff, there are notable differences in streamflow estimates among the experiments. While EXP4 demonstrated the best performance across all metrics in the evaluation of precipitation against GPM, its advantage in streamflow is primarily observed in terms of bias and in the Kling-

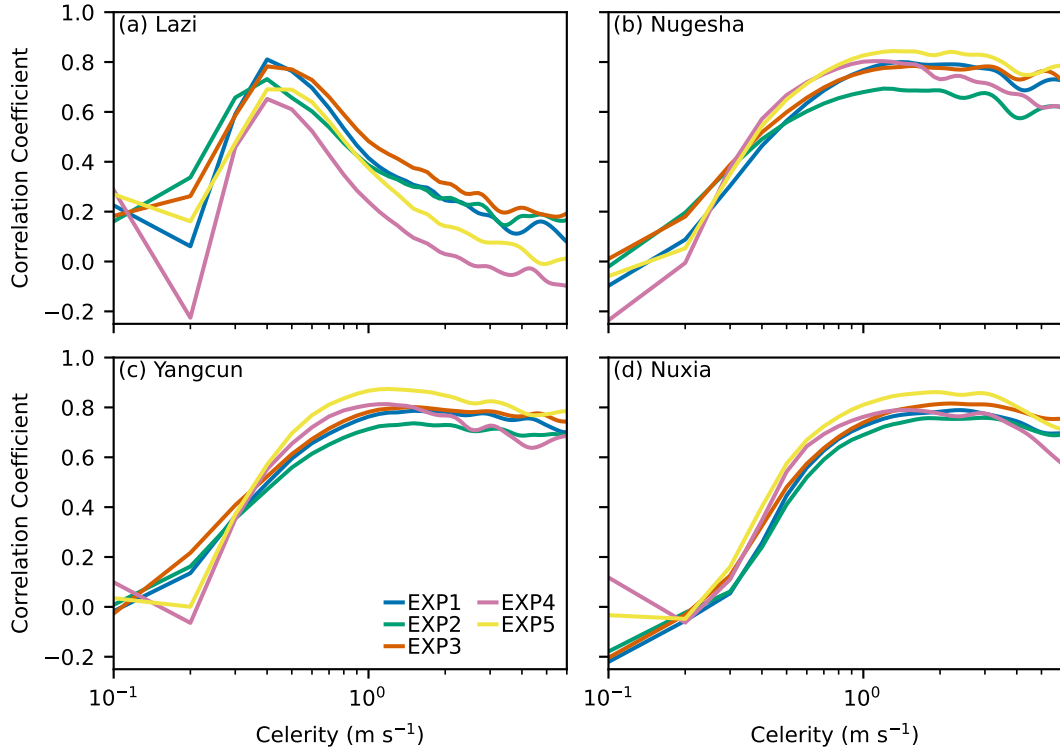


**Figure 6.** Sensitivity of streamflow modeling skill to wave celerity at the four river gauges:  
 (a) Lazi, (b) Nugesha, (c) Yangcun, and (d) Nuxia.

**Table 3.** The optimal flow wave celerity.

	LZ	NGS	YC	NX
EXP1	0.4	1.4	1.5	2.4
EXP2	0.4	1.2	1.5	3.0
EXP3	0.4	1.6	1.5	2.2
EXP4	0.4	1.1	1.2	1.5
EXP5	0.4	1.3	1.2	1.9

379 Gupta Efficiency (KGE) at the upper to middle reaches. The KGE value for EXP4 in-  
 380 creases progressively from upstream to downstream, with a value of -1.78 at the Lazi gauge  
 381 and improving to 0.69 at the Yangcun gauge. At the most downstream gauge, Nuxia,  
 382 EXP5 outperforms EXP4, achieving a KGE value of 0.70.

383 It is noteworthy that EXP5 outperforms EXP1 except at the upstream position  
 384 of the Yarlung Zangbo River at Lazi, even though their precipitation amounts are quite  
 385 similar. This superior performance of EXP5 is primarily attributed to the improved cor-  
 386 relation coefficient between the simulated and observed streamflow time series. We have  
 387 examined the relationship between the spatial correlation coefficient of streamflow and  
 388 the drainage basin-wide spatial correlation coefficient of precipitation, as depicted in Fig-  
 389 ure 8. With the exception of the Lazi drainage basin, a relatively high correspondence  
 390 in the temporal variations of streamflow is well-aligned with a relatively high correspon-  
 391 dence in the spatial distribution of precipitation. This alignment is a consequence of wa-  
 392 ter flow from various locations within the drainage basin converging at the outlet, which  
 393 influences the overall streamflow dynamics.

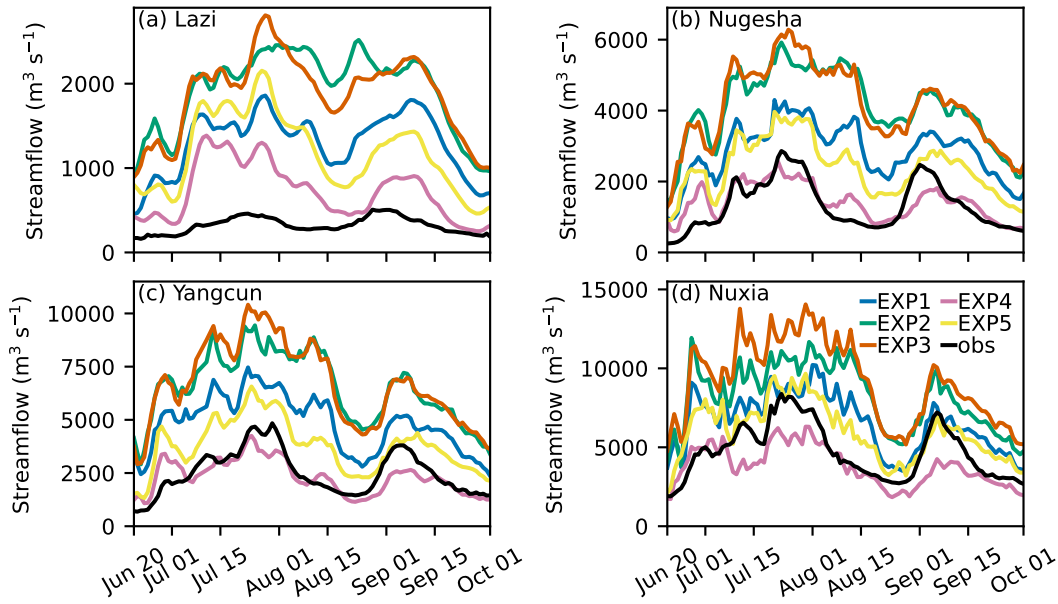


**Figure 7.** Comparison of streamflow observations with streamflow estimates from the WRF experiments.

## 394 4 Discussion

### 395 4.1 Impact of snowpack initialization

396 Previous studies have reported that ERA5 reanalysis data tend to overestimate snow  
 397 cover and snow water equivalent in high-altitude regions of the Tibetan Plateau, includ-  
 398 ing the Yarlung Zangbo River basin (Bian et al., 2019). Given that the initial condition

**Table 4.** Kling–Gupta efficiency of the optimal streamflow estimate.

	Metric	LZ	NGS	YC	NX
EXP1	KGE	−3.12	−0.16	0.01	0.54
	$\alpha$	3.76	1.14	1.26	1.06
	$\beta$	4.05	2.14	1.93	1.40
	$r$	0.81	0.80	0.79	0.79
EXP2	KGE	−5.34	−1.16	−0.72	0.19
	$\alpha$	4.88	1.51	1.57	1.23
	$\beta$	6.00	3.08	2.60	1.74
	$r$	0.73	0.69	0.74	0.76
EXP3	KGE	−5.24	−1.21	−0.88	−0.09
	$\alpha$	4.95	1.65	1.84	1.51
	$\beta$	5.82	3.11	2.67	1.95
	$r$	0.78	0.78	0.80	0.82
EXP4	KGE	−1.78	0.65	0.69	0.60
	$\alpha$	3.46	0.72	0.77	0.72
	$\beta$	2.25	1.07	0.93	0.81
	$r$	0.65	0.80	0.81	0.79
EXP5	KGE	−3.59	0.19	0.45	0.70
	$\alpha$	4.71	1.13	1.17	1.04
	$\beta$	3.68	1.79	1.51	1.27
	$r$	0.69	0.84	0.87	0.86

399 of the snowpack can significantly influence the simulations of land surface processes (F. Chen  
400 et al., 2014), we designated the first 50 days of the simulation period (from May 1 to June  
401 20) as a spin-up period to mitigate these potential biases. Consequently, only the results

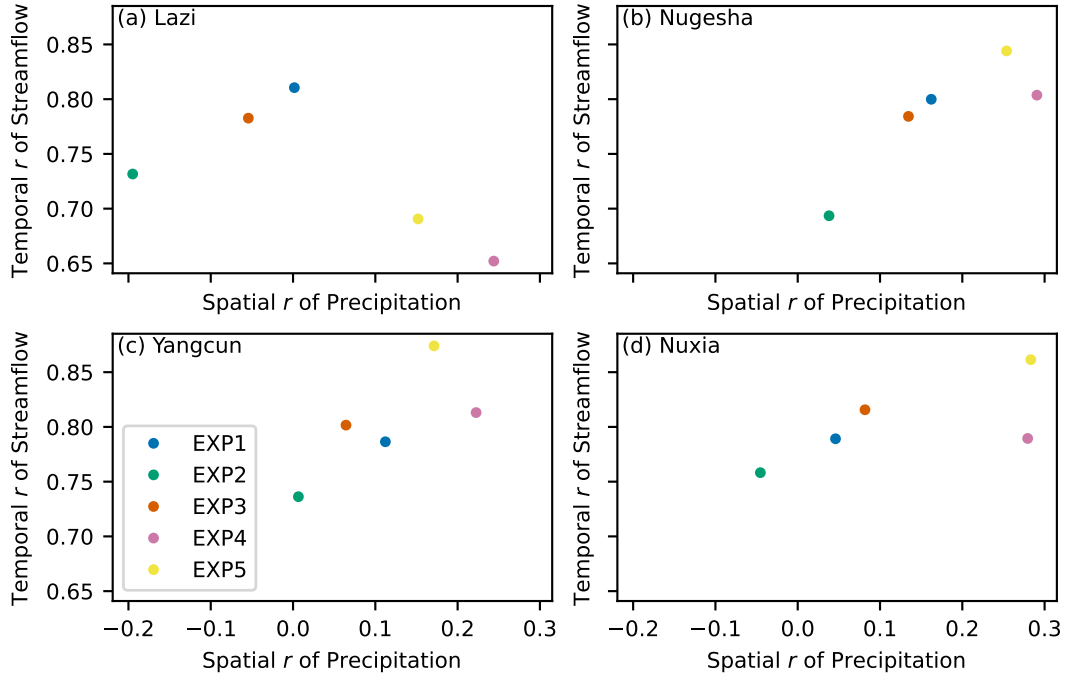


**Figure 8.** Relationship between the spatial correlation coefficient of precipitation and the temporal correlation coefficient of streamflow. (a) Streamflow observed at Lazi and precipitation averaged in the drainage basin of Lazi, (b) for Nugesha, (c) for Yangcun, and (d) for Nuxia.

from June 20 to October 1 were analyzed. However, it is possible that the effects of inaccurate snowpack initialization may still persist despite this approach.

To quantify any residual impact of snowpack initialization, we conducted an additional experiment, named SNOW, which employed the same parameterization schemes as EXP4 but initialized snow water equivalent (SWE) and snow depth using data from the Global Land Data Assimilation System (GLDAS) (Rodell et al., 2004). The GLDAS snow data, available at a spatial resolution of  $0.25^\circ$ , were bilinearly interpolated to match the WRF grid resolution. The celerity parameters were optimized following the procedure outlined in Figure 1.

Figure 9 presents a comparison of streamflow estimates between EXP4 and the additional SNOW experiment. The differences between these two experiments are negligible when compared to the differences observed between EXP1 and EXP4 (Figure 7). These results suggest that the 50-day spin-up period implemented in this study is sufficient to mitigate the impacts of snowpack initialization on the simulation results. In

416 this study, we focus on the evaluation of model parameterizations for warm-season sim-  
 417 ulations, where the influence of snowpack initialization is minimized through the use of  
 418 a long spin-up period. For cold-season simulations, where snowpack initialization plays  
 419 a crucial role, experiments with different initial conditions should be added to the inter-  
 420 comparison (as listed in Table 1). Our proposed method can then be used to eval-  
 421 uate the combination of different initial conditions and parameterization schemes.

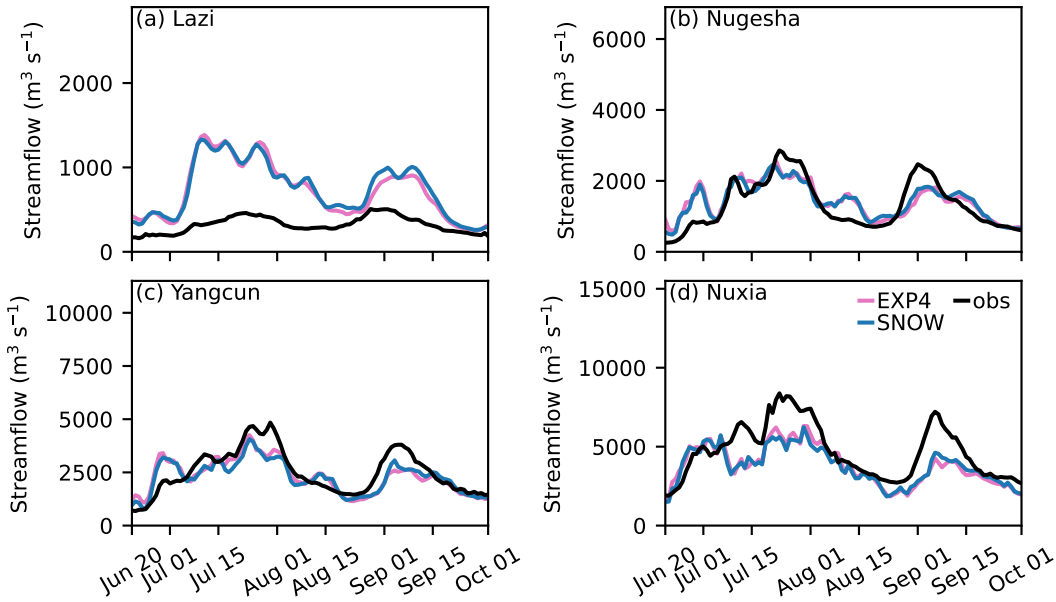


**Figure 9.** Impact of snowpack initialization on the simulated streamflow: (a) Streamflow at Lazi, (b) Nugesha, (c) Yangcun, and (d) Nuxia.

#### 422 4.2 Impact of terrain routing

423 In this study, we kept the routing model as simple as possible to avoid overparam-  
 424 eterization and did not include a dedicated terrain routing model. To evaluate the im-  
 425 pact of omitting terrain routing, we delineated an alternative river network using a drainage  
 426 area threshold of  $1 \text{ km}^2$ . The rivers within the network were further divided into  $1\text{-km}^2$   
 427 reaches, resulting in a dense river network comprising 194,171 reaches, with an average  
 428 catchment area of approximately  $1 \text{ km}^2$  per reach. On the southeastern edge of the Ti-  
 429 betan Plateau, terrain routing within such small catchments can be safely neglected. We  
 430 then routed the runoff from EXP4 on this high-resolution river network, with celerity  
 431 parameters set to the same values used in EXP4.

432 Figure 10 shows the time series of streamflow estimates from EXP4 and from the  
 433 high-resolution river network (referred to as HIRES). The differences between these two  
 434 experiments are marginal compared to the differences among EXP1 to EXP4 (Figure 7).  
 435 These results indicate that terrain routing can be neglected in this study without sig-  
 436 nificantly affecting the results. This simplification significantly reduces the computational  
 437 cost of parameter optimization and streamlines the model structure while maintaining  
 438 the robustness of the evaluation.

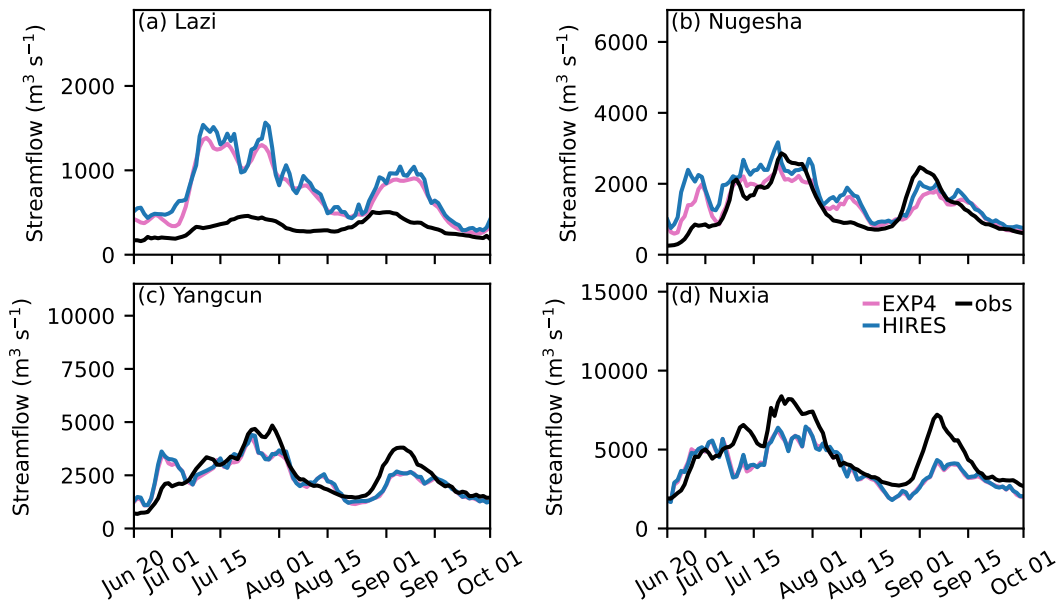


**Figure 10.** Comparison of streamflow simulated from EXP4 and from the high-resolution river network delineated with a drainage area threshold of 1 km<sup>2</sup> and river reach length of 1 km.  
 (a) Observed and simulated streamflow at Lazi, (b) Nugesha, (c) Yangcun, and (d) Nuxia.

## 439 5 Conclusions

440 We have proposed a river network routing-based method for evaluating atmospheric  
 441 models using streamflow observations. This method stands out from the hydrological model-  
 442 based approach by relying on a substantially smaller set of assumptions regarding model  
 443 structures and parameters. The streamlined nature of this approach enhances its robust-  
 444 ness and makes it a more attractive alternative compared to hydrological model-based  
 445 evaluations. This is particularly relevant in mountainous basins, where hydrological mod-  
 446 els often struggle to accurately capture the complexities of runoff-generation processes.

We applied this method to evaluate five numerical experiments, each featuring different configurations of WRF, in the simulated streamflow of the Yarlung Zangbo River, the largest river on the Tibetan Plateau. The streamflow evaluation complements the precipitation evaluation utilizing the GPM precipitation product. Our results indicate a consistency between the proposed method's outcomes and those derived from the precipitation evaluation. Notably, the WRF configuration that integrated the Thompson cloud microphysics scheme, the RRTMG radiation scheme, and the YSU planetary boundary layer scheme exhibited optimal performance in simulating precipitation. This configuration's enhanced capability to replicate both the total amount and temporal patterns of precipitation is crucial for accurately estimating the mean and variability of streamflow.

Our proposed method enriches the evaluation of precipitation. While the shortwave radiation transfer process was found to have a minimal impact on the total amount of precipitation during the initial evaluation, it exerts a significant influence on streamflow simulation, particularly in the middle reaches between Lazi and Yangcun. Notably, the experiment that employed the Dudhia radiation scheme excelled in terms of the correlation coefficient and the Kling–Gupta Efficiency (KGE) at the downstream Nuxia gauge. This superior performance in modeling streamflow time series is attributed to the Dudhia scheme's effectiveness in capturing the spatial distribution of precipitation, underscoring the importance of accurate radiation transfer modeling in streamflow simulation. These findings reinforce the significance of the precipitation gradient in mountainous hydrology, as discussed in (Immerzeel et al., 2014), and demonstrate the potential of our proposed method in evaluating atmospheric models in mountainous basins.

In-situ meteorological observations often suffer from limited spatial representation in mountainous regions such as the Tibetan Plateau (Miao et al., 2024). Numerical models and hydrological observations are considered advantageous in such cases. It has been found that numerical models can better capture spatial variability and outperform in-situ meteorological observations (Lundquist et al., 2019), whereas hydrological observations can represent hydrometeorological conditions over the entire drainage basin. This study serves as an example of combining numerical models and hydrological observations, highlighting the usefulness of integrating river network routing into regional models. This study can lay a foundation for future research that incorporates more advanced techniques, such as data assimilation, Bayesian inference, and machine learning, to further improve

480 the estimation and forecasting of hydrometeorological conditions in mountainous regions.  
 481 The data and code used in this study are publicly available, facilitating future research  
 482 in this direction.

#### 483 Open Research Section

484 The GPM IMERG final run precipitation product version 6 was used to evaluate  
 485 the WRF-simulated precipitation (Huffman et al., 2019). The ERA5 reanalysis data (Hersbach  
 486 et al., 2020) were used to drive the WRF model version 4.3.1 (Powers et al., 2017) to sim-  
 487 ulate precipitation and runoff. The MERIT-Hydro flow direction and cumulative upstream  
 488 area data (Yamazaki et al., 2019) were used to delineate the river network. The delin-  
 489 eated river network, WRF-simulated precipitation and runoff, and the code for routing  
 490 and parameter optimization are available at [https://doi.org/10.57760/sciencedb](https://doi.org/10.57760/sciencedb.11618)  
 491 .11618 (Zheng et al., 2024). The streamflow observations for the Yarlung Zangbo River  
 492 were obtained from China Three Gorges Corporation; however, they are not shareable  
 493 due to licensing restrictions.

#### 494 Acknowledgments

495 This study is supported by the National Key Research and Development Program  
 496 of China (2023YFF0805501), China Yangtze Power Co., Ltd. (contract Z532302035), and  
 497 the Natural Science Foundation of China (grants 42075165 and 42275178).

#### 498 References

- 499 Behrangi, A., Andreadis, K., Fisher, J. B., Turk, F. J., Granger, S., Painter, T.,  
 500 & Das, N. (2014). Satellite-based precipitation estimation and its ap-  
 501 plication for streamflow prediction over mountainous western U.S. basins.  
 502 *Journal of Applied Meteorology and Climatology*, 53(12), 2823–2842. doi:  
 503 10.1175/JAMC-D-14-0056.1
- 504 Bian, Q., Xu, Z., Zhao, L., Zhang, Y.-F., Zheng, H., Shi, C., ... Yang, Z.-L. (2019).  
 505 Evaluation and intercomparison of multiple snow water equivalent products  
 506 over the tibetan plateau. *Journal of Hydrometeorology*, 20(10), 2043–2055. doi:  
 507 10.1175/JHM-D-19-0011.1
- 508 Chen, F., Liu, C., Dudhia, J., & Chen, M. (2014). A sensitivity study of high-  
 509 resolution regional climate simulations to three land surface models over the

- 510 western United State. *Journal of Geophysical Research: Atmospheres*, 119(12),  
511 7271–7291. doi: 10.1002/2014JD021827
- 512 Chen, S.-H., & Sun, W.-Y. (2002). A one-dimensional time dependent cloud model.  
513 *Journal of the Meteorological Society of Japan. Ser. II*, 80(1), 99–118. doi: 10  
514 .2151/jmsj.80.99
- 515 Clark, M. P., Kavetski, D., & Fenicia, F. (2011). Pursuing the method of multi-  
516 ple working hypotheses for hydrological modeling. *Water Resources Research*,  
517 47(9), 1–16. doi: 10.1029/2010WR009827
- 518 Clark, P., Roberts, N., Lean, H., Ballard, S. P., & Charlton-Perez, C. (2016).  
519 Convection-permitting models: a step-change in rainfall forecasting. *Meteo-*  
520 *logical Applications*, 23(2), 165–181. doi: 10.1002/met.1538
- 521 Cosgrove, B., Gochis, D., Flowers, T., Dugger, A., Ogden, F., Graziano, T., ...  
522 Zhang, Y. (2024). NOAA’s National Water Model: Advancing operational  
523 hydrology through continental-scale modeling. *Journal of the American Water  
524 Resources Association*, 60(2), 247–272. doi: 10.1111/1752-1688.13184
- 525 Cui, T., Li, Y., Yang, L., Nan, Y., Li, K., Tudaji, M., ... Tian, F. (2023).  
526 Non-monotonic changes in Asian Water Towers’ streamflow at increas-  
527 ing warming levels. *Nature Communications*, 14(1), 1176. doi: 10.1038/  
528 s41467-023-36804-6
- 529 Cunge, J. A. (1969). On the subject of a flood propagation computation method  
530 (Muskingum method). *Journal of Hydraulic Research*, 7(2), 205–230. doi: 10  
531 .1080/00221686909500264
- 532 David, C. H., Maidment, D. R., Niu, G.-Y., Yang, Z.-L., Habets, F., & Eikhout, V.  
533 (2011). River network routing on the NHDPlus dataset. *Journal of Hydrome-  
534 teorology*, 12(5), 913–934. doi: 10.1175/2011JHM1345.1
- 535 Denis, B., Laprise, R., Caya, D., & Côté, J. (2002). Downscaling ability of one-way  
536 nested regional climate models: the Big-Brother Experiment. *Climate Dynam-  
537 ics*, 18(8), 627–646. doi: 10.1007/s00382-001-0201-0
- 538 Dudhia, J. (1989). Numerical study of convection observed during the winter  
539 monsoon experiment using a mesoscale two-dimensional model. *Journal of  
540 the Atmospheric Sciences*, 46(20), 3077–3107. doi: 10.1175/1520-0469(1989)  
541 046<3077:NSOCOD>2.0.CO;2
- 542 Fenton, J. D. (2019). Flood routing methods. *Journal of Hydrology*, 570, 251–264.

- 543 doi: 10.1016/j.jhydrol.2019.01.006
- 544 Getirana, A. C., & Paiva, R. C. (2013). Mapping large-scale river flow hydraulics  
545 in the Amazon Basin. *Water Resources Research*, 49(5), 2437–2445. doi: 10  
546 .1002/wrcr.20212
- 547 Givati, A., Gochis, D., Rummler, T., & Kunstmann, H. (2016). Comparing  
548 one-way and two-way coupled hydrometeorological forecasting systems for  
549 flood forecasting in the Mediterranean region. *Hydrology*, 3(2), 19. doi:  
550 10.3390/hydrology3020019
- 551 Gupta, H. V., Kling, H., Yilmaz, K. K., & Martinez, G. F. (2009). Decomposition  
552 of the mean squared error and NSE performance criteria: Implications for im-  
553 proving hydrological modelling. *Journal of Hydrology*, 377(1-2), 80–91. doi:  
554 10.1016/j.jhydrol.2009.08.003
- 555 Henn, B., Clark, M. P., Kavetski, D., & Lundquist, J. D. (2015). Estimating moun-  
556 tain basin-mean precipitation from streamflow using Bayesian inference. *Water  
557 Resources Research*, 51(10), 8012–8033. doi: 10.1002/2014WR016736
- 558 Henn, B., Clark, M. P., Kavetski, D., McGurk, B., Painter, T. H., & Lundquist,  
559 J. D. (2016). Combining snow, streamflow, and precipitation gauge observa-  
560 tions to infer basin-mean precipitation. *Water Resources Research*, 52(11),  
561 8700–8723. doi: 10.1002/2015WR018564
- 562 Hersbach, H., Bell, B., Berrisford, P., Hirahara, S., Horányi, A., Muñoz-Sabater, J.,  
563 ... Thépaut, J.-N. (2020). The ERA5 global reanalysis. *Quarterly Journal of  
564 the Royal Meteorological Society*, 146(730), 1999–2049. doi: 10.1002/qj.3803
- 565 Hong, S.-Y., & Lim, J.-O. J. (2006). The WRF Single-Moment 6-Class Microphysics  
566 Scheme (WSM6). *Asia-Pacific Journal of Atmospheric Sciences*, 42(2), 129–  
567 151.
- 568 Hong, S.-Y., Noh, Y., & Dudhia, J. (2006). A new vertical diffusion package with an  
569 explicit treatment of entrainment processes. *Monthly Weather Review*, 134(9),  
570 2318–2341. doi: 10.1175/MWR3199.1
- 571 Huffman, G. J., Stocker, E. F., Bolvin, D. T., Nelkin, E. J., & Tan, J. (2019).  
572 *GPM IMERG final precipitation L3 half hourly 0.1 degree x 0.1 degree V06*  
573 (*GPM\_3IMERGHH*). NASA/GSFC/SED/ESD/GCDC/GESDISC. Retrieved  
574 2022-12-05, from <https://doi.org/10.5067/GPM/IMERG/3B-HH/06> doi:  
575 10.5067/GPM/IMERG/3B-HH/06

- 576 Iacono, M. J., Delamere, J. S., Mlawer, E. J., Shephard, M. W., Clough, S. A., &  
577 Collins, W. D. (2008). Radiative forcing by long-lived greenhouse gases: Calculations with the AER radiative transfer models. *Journal of Geophysical*  
578 *Research: Atmospheres*, 113(D13), D13103. doi: 10.1029/2008JD009944
- 580 Immerzeel, W. W., Petersen, L., Ragettli, S., & Pellicciotti, F. (2014). The importance  
581 of observed gradients of air temperature and precipitation for modeling runoff from a glacierized watershed in the Nepalese Himalayas. *Water Re-*  
582 *sources Research*, 50(3), 2212–2226. doi: 10.1002/2013WR014506
- 584 Janjić, Z. I. (1994). The step-mountain Eta coordinate model: further developments  
585 of the convection, viscous sublayer, and turbulence closure schemes. *Monthly*  
586 *Weather Review*, 122(5), 927–945. doi: 10.1175/1520-0493(1994)122<0927:  
587 TSMECM>2.0.CO;2
- 588 Jiang, Y., Yang, K., Li, X., Zhang, W., Shen, Y., Chen, Y., & Li, X. (2022).  
589 Atmospheric simulation-based precipitation datasets outperform satellite-  
590 based products in closing basin-wide water budget in the eastern Tibetan  
591 Plateau. *International Journal of Climatology*, 42(14), 7252–7268. doi:  
592 10.1002/joc.7642
- 593 Jiang, Y., Yang, K., Yang, H., Lu, H., Chen, Y., Zhou, X., ... Wang, Y. (2022).  
594 Characterizing basin-scale precipitation gradients in the Third Pole region  
595 using a high-resolution atmospheric simulation-based dataset. *Hydrology and*  
596 *Earth System Sciences*, 26(17), 4587–4601. doi: 10.5194/hess-26-4587-2022
- 597 Kirchner, J. W. (2009). Catchments as simple dynamical systems: Catchment char-  
598 acterization, rainfall-runoff modeling, and doing hydrology backward. *Water*  
599 *Resources Research*, 45(2), W02429. doi: 10.1029/2008WR006912
- 600 Koussis, A. D. (1978). Theoretical estimation of flood routing parameters. *Journal*  
601 *of the Hydraulics Division*, 104(1), 109–115. doi: 10.1061/JYCEAJ.0004909
- 602 Kraaijenbrink, P. D. A., Stigter, E. E., Yao, T., & Immerzeel, W. W. (2021).  
603 Climate change decisive for Asia's snow meltwater supply. *Nature Climate*  
604 *Change*, 11(7), 591–597. doi: 10.1038/s41558-021-01074-x
- 605 Krier, R., Matgen, P., Goergen, K., Pfister, L., Hoffmann, L., Kirchner, J. W., ...  
606 Savenije, H. H. G. (2012). Inferring catchment precipitation by doing hydrology  
607 backward: A test in 24 small and mesoscale catchments in Luxembourg.  
608 *Water Resources Research*, 48(10), W10525. doi: 10.1029/2011WR010657

- 609 Kukulies, J., Prein, A. F., Curio, J., Yu, H., & Chen, D. (2023). Kilometer-scale  
610 multimodel and multiphysics ensemble simulations of a mesoscale convective  
611 system in the lee of the Tibetan Plateau: implications for climate simulations.  
612 *Journal of Climate*, 36(17), 5963–5987. doi: 10.1175/JCLI-D-22-0240.1
- 613 Lei, X., Lin, P., Zheng, H., Fei, W., Yin, Z., & Ren, H. (2025). Systematic anal-  
614 yses of the meteorological forcing and process parameterization uncertainties  
615 in modeling runoff with Noah-MP for the Upper Brahmaputra river basin.  
616 *Journal of Hydrology*, 653, 132686. doi: 10.1016/j.jhydrol.2025.132686
- 617 Li, G., Chen, H., Xu, M., Zhao, C., Zhong, L., Li, R., ... Gao, Y. (2022). Impacts of  
618 topographic complexity on modeling moisture transport and precipitation over  
619 the Tibetan Plateau in summer. *Advances in Atmospheric Sciences*, 39(7),  
620 1151–1166. doi: 10.1007/s00376-022-1409-7
- 621 Li, L., Bisht, G., Hao, D., & Leung, L. R. (2024). Global 1 km land surface param-  
622 eters for kilometer-scale Earth system modeling. *Earth System Science Data*,  
623 16(4), 2007–2032. doi: 10.5194/essd-16-2007-2024
- 624 Liang, J., Yang, Z.-L., & Lin, P. (2019). Systematic hydrological evaluation of the  
625 Noah-MP land surface model over China. *Advances in Atmospheric Sciences*,  
626 36(11), 1171–1187. doi: 10.1007/s00376-019-9016-y
- 627 Lin, C., Chen, D., Yang, K., & Ou, T. (2018). Impact of model resolution on sim-  
628 ulating the water vapor transport through the central Himalayas: implication  
629 for models' wet bias over the Tibetan Plateau. *Climate Dynamics*, 51(9),  
630 3195–3207. doi: 10.1007/s00382-018-4074-x
- 631 Lin, P., Hopper, L. J., Yang, Z.-L., Lenz, M., & Zeitler, J. W. (2018). Insights into  
632 hydrometeorological factors constraining flood prediction skill during the May  
633 and October 2015 Texas Hill Country flood events. *Journal of Hydrometeorol-  
634 ogy*, 19(8), 1339–1361. doi: 10.1175/JHM-D-18-0038.1
- 635 Lin, P., Pan, M., Beck, H. E., Yang, Y., Yamazaki, D., Frasson, R., ... Wood, E. F.  
636 (2019). Global reconstruction of naturalized river flows at 2.94 million reaches.  
637 *Water Resources Research*, 55(8), 6499–6516. doi: 10.1029/2019WR025287
- 638 Lin, P., Pan, M., Wood, E. F., Yamazaki, D., & Allen, G. H. (2021). A new vector-  
639 based global river network dataset accounting for variable drainage density.  
640 *Scientific Data*, 8(1), 28. doi: 10.1038/s41597-021-00819-9
- 641 Lin, P., Yang, Z.-L., Gochis, D. J., Yu, W., Maidment, D. R., Somos-Valenzuela,

- 642 M. A., & David, C. H. (2018). Implementation of a vector-based river network  
 643 routing scheme in the community WRF-Hydro modeling framework for flood  
 644 discharge simulation. *Environmental Modelling & Software*, 107, 1–11. doi:  
 645 10.1016/j.envsoft.2018.05.018
- 646 Lundquist, J., Hughes, M., Gutmann, E., & Kapnick, S. (2019). Our skill in mod-  
 647eling mountain rain and snow is bypassing the skill of our observational net-  
 648 works. *Bulletin of the American Meteorological Society*, 100(12), 2473–2490.  
 649 doi: 10.1175/bams-d-19-0001.1
- 650 Lv, M., Xu, Z., & Yang, Z. (2020). Cloud resolving WRF simulations of precipi-  
 651 tation and soil moisture over the central Tibetan Plateau: an assessment of  
 652 various physics options. *Earth and Space Science*, 7(2), e2019EA000865. doi:  
 653 10.1029/2019EA000865
- 654 Ma, M., Ou, T., Liu, D., Wang, S., Fang, J., & Tang, J. (2023). Summer re-  
 655 gional climate simulations over Tibetan Plateau: from gray zone to con-  
 656 vection permitting scale. *Climate Dynamics*, 60(1), 301–322. doi:  
 657 10.1007/s00382-022-06314-0
- 658 Miao, C., Immerzeel, W. W., Xu, B., Yang, K., Duan, Q., & Li, X. (2024). Un-  
 659 derstanding the Asian water tower requires a redesigned precipitation obser-  
 660 vation strategy. *Proceedings of the National Academy of Sciences*, 121(23),  
 661 e2403557121. doi: 10.1073/pnas.2403557121
- 662 Mlawer, E. J., Taubman, S. J., Brown, P. D., Iacono, M. J., & Clough, S. A. (1997).  
 663 Radiative transfer for inhomogeneous atmospheres: RRTM, a validated  
 664 correlated-k model for the longwave. *Journal of Geophysical Research: At-*  
*665 mospheres*, 102(D14), 16663–16682. doi: 10.1029/97JD00237
- 666 Mooney, P. A., Broderick, C., Bruyère, C. L., Mulligan, F. J., & Prein, A. F. (2017).  
 667 Clustering of observed diurnal cycles of precipitation over the United States  
 668 for evaluation of a WRF multiphysics regional climate ensemble. *Journal of*  
*669 Climate*, 30(22), 9267–9286. doi: 10.1175/JCLI-D-16-0851.1
- 670 Moussa, R., & Bocquillon, C. (1996). Criteria for the choice of flood-routing meth-  
 671 ods in natural channels. *Journal of Hydrology*, 186(1-4), 1–30. doi: 10.1016/  
 672 S0022-1694(96)03045-4
- 673 Niu, G.-Y., Yang, Z.-L., Mitchell, K. E., Chen, F., Ek, M. B., Barlage, M., ... Xia,  
 674 Y. (2011). The community Noah land surface model with multiparameteriza-

- 675 tion options (Noah-MP): 1. Model description and evaluation with local-scale  
676 measurements. *Journal of Geophysical Research: Atmospheres*, 116(D12),  
677 D12109. doi: 10.1029/2010JD015139
- 678 Pang, J., Zhang, H., Xu, Q., Wang, Y., Wang, Y., Zhang, O., & Hao, J. (2020).  
679 Hydrological evaluation of open-access precipitation data using SWAT at mul-  
680 tiple temporal and spatial scales. *Hydrology and Earth System Sciences*, 24(7),  
681 3603–3626. doi: 10.5194/hess-24-3603-2020
- 682 Ponce, V. M., Simons, D. B., & Li, R.-M. (1978). Applicability of kinematic and dif-  
683 fusion models. *Journal of the Hydraulics Division*, 104(3), 353–360. doi: 10  
684 .1061/JYCEAJ.0004958
- 685 Powers, J. G., Klemp, J. B., Skamarock, W. C., Davis, C. A., Dudhia, J., Gill,  
686 D. O., ... Duda, M. G. (2017). The Weather Research and Forecasting model:  
687 overview, system efforts, and future directions. *Bulletin of the American Mete-  
688 orological Society*, 98(8), 1717–1737. doi: 10.1175/bams-d-15-00308.1
- 689 Prein, A. F., Ban, N., Ou, T., Tang, J., Sakaguchi, K., Collier, E., ... Chen,  
690 D. (2023). Towards ensemble-based kilometer-scale climate simulations  
691 over the Third Pole region. *Climate Dynamics*, 60(11), 4055–4081. doi:  
692 10.1007/s00382-022-06543-3
- 693 Prein, A. F., Langhans, W., Fosser, G., Ferrone, A., Ban, N., Goergen, K., ... Le-  
694 ung, R. (2015). A review on regional convection-permitting climate modeling:  
695 Demonstrations, prospects, and challenges. *Reviews of Geophysics*, 53(2),  
696 323–361. doi: 10.1002/2014RG000475
- 697 RafieeiNasab, A., Fienen, M. N., Oman, N., Srivastava, I., & Dugger, A. L. (2025).  
698 Ensemble methods for parameter estimation of WRF-hydro. *Water Resources  
699 Research*, 61(1), e2024WR038048. doi: 10.1029/2024WR038048
- 700 Renard, B., Kavetski, D., Kuczera, G., Thyre, M., & Franks, S. W. (2010). Un-  
701 derstanding predictive uncertainty in hydrologic modeling: The challenge of  
702 identifying input and structural errors. *Water Resources Research*, 46(5),  
703 W05521. doi: 10.1029/2009WR008328
- 704 Rodell, M., Houser, P. R., Jambor, U., Gottschalck, J., Mitchell, K., Meng,  
705 C.-J., ... Toll, D. (2004). The global land data assimilation system.  
706 *Bulletin of the American Meteorological Society*, 85(3), 381–394. doi:  
707 10.1175/BAMS-85-3-381

- 708 Schaake, J. C., Koren, V. I., Duan, Q.-Y., Mitchell, K., & Chen, F. (1996). Simple  
709 water balance model for estimating runoff at different spatial and temporal  
710 scales. *Journal of Geophysical Research: Atmospheres*, 101(D3), 7461–7475.  
711 doi: 10.1029/95JD02892
- 712 Senatore, A., Mendicino, G., Gochis, D. J., Yu, W., Yates, D. N., & Kunstmann,  
713 H. (2015). Fully coupled atmosphere-hydrology simulations for the central  
714 Mediterranean: Impact of enhanced hydrological parameterization for short  
715 and long time scales. *Journal of Advances in Modeling Earth Systems*, 7(4),  
716 1693–1715. doi: 10.1002/2015MS000510
- 717 Stevens, B., Satoh, M., Auger, L., Biercamp, J., Bretherton, C. S., Chen, X., ...  
718 Zhou, L. (2019). DYAMOND: the DYnamics of the Atmospheric general circu-  
719 lation Modeled On Non-hydrostatic Domains. *Progress in Earth and Planetary  
720 Science*, 6(1), 61. doi: 10.1186/s40645-019-0304-z
- 721 Sugimoto, S., Ueno, K., Fujinami, H., Nasuno, T., Sato, T., & Takahashi, H. G.  
722 (2021). Cloud-resolving-model simulations of nocturnal precipitation over  
723 the Himalayan slopes and foothills. *Journal of Hydrometeorology*, 22(12),  
724 3171–3188. doi: 10.1175/JHM-D-21-0103.1
- 725 Tang, Q., Golaz, J.-C., Van Roekel, L. P., Taylor, M. A., Lin, W., Hillman, B. R.,  
726 ... Bader, D. C. (2023). The fully coupled regionally refined model of E3SM  
727 version 2: overview of the atmosphere, land, and river results. *Geoscientific  
728 Model Development*, 16(13), 3953–3995. doi: 10.5194/gmd-16-3953-2023
- 729 Thompson, G., Field, P. R., Rasmussen, R. M., & Hall, W. D. (2008). Explicit fore-  
730 casts of winter precipitation using an improved bulk microphysics scheme. part  
731 II: implementation of a new snow parameterization. *Monthly Weather Review*,  
732 136(12), 5095–5115. doi: 10.1175/2008MWR2387.1
- 733 van Tiel, M., Aubry-Wake, C., Somers, L., Andermann, C., Avanzi, F., Baraer, M.,  
734 ... Yapiyev, V. (2024). Cryosphere-groundwater connectivity is a miss-  
735 ing link in the mountain water cycle. *Nature Water*, 2(7), 624–637. doi:  
736 10.1038/s44221-024-00277-8
- 737 Wagner, S., Fersch, B., Yuan, F., Yu, Z., & Kunstmann, H. (2016). Fully coupled  
738 atmospheric-hydrological modeling at regional and long-term scales: Devel-  
739 opment, application, and analysis of WRF-HMS. *Water Resources Research*,  
740 52(4), 3187–3211. doi: 10.1002/2015wr018185

- 741 Wang, S., Zheng, H., Lin, P., Zheng, X., & Yang, Z.-L. (2019). Evaluation and un-  
742 certainty attribution of the simulated streamflow from NoahMP-RAPID over a  
743 high-altitude mountainous basin. *Chinese Science Bulletin (in Chinese)*, 64(4),  
744 444–455. doi: 10.1360/N972018-00598
- 745 Wang, T., Zhao, Y., Xu, C., Ciais, P., Liu, D., Yang, H., ... Yao, T. (2021).  
746 Atmospheric dynamic constraints on Tibetan Plateau freshwater under  
747 Paris climate targets. *Nature Climate Change*, 11(3), 219–225. doi:  
748 10.1038/s41558-020-00974-8
- 749 Wang, X., Tolksdorf, V., Otto, M., & Scherer, D. (2021). WRF-based dynamical  
750 downscaling of ERA5 reanalysis data for High Mountain Asia: Towards a new  
751 version of the High Asia Refined analysis. *International Journal of Climatol-  
752 ogy*, 41(1), 743–762. doi: 10.1002/joc.6686
- 753 Wang, Y., Zeng, X., Xu, X., Welty, J., Lenschow, D. H., Zhou, M., & Zhao, Y.  
754 (2020). Why are there more summer afternoon low clouds over the Tibetan  
755 Plateau compared to Eastern China? *Geophysical Research Letters*, 47(23),  
756 e2020GL089665. doi: 10.1029/2020gl089665
- 757 Yamazaki, D., Ikeshima, D., Sosa, J., Bates, P. D., Allen, G. H., & Pavelsky, T. M.  
758 (2019). MERIT Hydro: A high-resolution global hydrography map based on  
759 latest topography dataset. *Water Resources Research*, 55(6), 5053–5073. doi:  
760 10.1029/2019wr024873
- 761 Yamazaki, D., Ikeshima, D., Tawatari, R., Yamaguchi, T., O'Loughlin, F., Neal,  
762 J. C., ... Bates, P. D. (2017). A high-accuracy map of global ter-  
763 rain elevations. *Geophysical Research Letters*, 44(11), 5844–5853. doi:  
764 10.1002/2017GL072874
- 765 Yang, X., Wei, C., Li, Z., Yang, H., & Zheng, H. (2024). A stream-order family and  
766 order-based parallel river network routing method. *Water*, 16(14), 1965. doi:  
767 10.3390/w16141965
- 768 Yang, Z.-L., Niu, G.-Y., Mitchell, K. E., Chen, F., Ek, M. B., Barlage, M., ...  
769 Xia, Y. (2011). The community Noah land surface model with multipa-  
770 rameterization options (Noah-MP): 2. Evaluation over global river basins.  
771 *Journal of Geophysical Research: Atmospheres*, 116(D12), D12110. doi:  
772 10.1029/2010JD015140
- 773 Yao, T., Xue, Y., Chen, D., Chen, F., Thompson, L., Cui, P., ... Li, Q. (2019).

- 774       Recent Third Pole's rapid warming accompanies cryospheric melt and wa-  
775       ter cycle intensification and interactions between monsoon and environ-  
776       ment: multidisciplinary approach with observations, modeling, and analy-  
777       sis.     *Bulletin of the American Meteorological Society*, 100(3), 423–444.   doi:  
778       10.1175/bams-d-17-0057.1
- 779       Yuan, X., Yang, K., Lu, H., Wang, Y., & Ma, X. (2023). Impacts of moisture trans-  
780       port through and over the Yarlung Tsangpo Grand Canyon on precipitation  
781       in the eastern Tibetan Plateau.     *Atmospheric Research*, 282, 106533.   doi:  
782       10.1016/j.atmosres.2022.106533
- 783       Zheng, H., Fei, W., Yang, Z.-L., Wei, J., Zhao, L., Li, L., & Wang, S. (2023). An  
784       ensemble of 48 physically perturbed model estimates of the 1/8° terrestrial  
785       water budget over the conterminous United States, 1980–2015.     *Earth System*  
786       *Science Data*, 15(7), 2755–2780. doi: 10.5194/essd-15-2755-2023
- 787       Zheng, H., Yang, H., & Chen, S. (2024).     *Evaluating atmospheric model pa-*  
788       *rameterization schemes with river network routing and streamflow obser-*  
789       *vations: A case study of the Yarlung Zangbo River on the Tibetan Plateau.*  
790       <https://www.scidb.cn>: Science Data Bank. doi: 10.57760/sciedb.11618
- 791       Zheng, H., Yang, Z.-L., Lin, P., Wu, W.-Y., Li, L., Xu, Z., ... Wang, S. (2020).  
792       Falsification-oriented signature-based evaluation for guiding the develop-  
793       ment of land surface models and the enhancement of observations.     *Jour-*  
794       *nal of Advances in Modeling Earth Systems*, 12(12), e2020MS002132.   doi:  
795       10.1029/2020MS002132
- 796       Zhou, X., Yang, K., Ouyang, L., Wang, Y., Jiang, Y., Li, X., ... Prein, A. (2021).  
797       Added value of kilometer-scale modeling over the third pole region: a  
798       CORDEX-CPTP pilot study.     *Climate Dynamics*, 57(7), 1673–1687.   doi:  
799       10.1007/s00382-021-05653-8